A New Mechanics Model for Continuum Notched-Tube Wrists that Accounts for Tendon Friction and Material Nonlinearities

by

Nicholas E. Pacheco

A Thesis

Submitted to the Faculty

of the

WORCESTER POLYTECHNIC INSTITUTE

In partial fulfillment of the requirements for the

Degree of Master of Science

in

Robotics Engineering

May 2021

APPROVED BY:

Prof. Loris Fichera, Major Thesis Advisor

Prof. Cagdas Onal, Thesis Committee Member

Dr. Joshua Gafford, Thesis Committee Member

Abstract

In this thesis, we present a new mechanics model for notched-tube continuum wrists, a class of mechanisms frequently used to implement distal steering in needle-sized surgical robotic instruments. Existing kinematic models available for these devices use two simplifying assumptions, namely (*i*) frictionless actuation and (*ii*) linear material properties, so that wrist bending can be treated as a purely geometric problem. This approach is analytically attractive, but, as we show in this thesis, it can sometimes fail to provide good tracking accuracy. The model proposed in this thesis relaxes both of the assumptions above, and provides superior accuracy compared to previous models. Wrist deflection is estimated using Castigliano's second theorem, with the addition of a capstan friction term that models frictional losses on the actuation tendon. Because notched-tube wrists are typically made of Nickel-Titanium (Nitinol), which has nonlinear stress-strain characteristics, we introduce a technique to obtain a local linearized approximation of the material modulus, suitable for use in the deflection model. The result of our modeling is a system of nonlinear equations that can be solved numerically to predict the wrist configuration based on the applied actuation force. Experimental validation was performed on manufactured notched-tube continuum wrists. Our model had an average Root-Mean-Square error of only 1 degree per notch and we show that our model has an average tip position Root-Mean-Square error of only 0.3 millimeters where models with tighter assumptions have greater errors around 0.73 millimeters on average.

Acknowledgements

I would first like to thank my advisor, Professor Loris Fichera, who was always available to discuss my work and provide me with feedback. His counsel went beyond the scope of this thesis and helped me be a better researcher. I am grateful to my thesis committee, Professor Cagdas Onal and Dr. Joshua Gafford, for their guidance and time spent reviewing my work. I'd like to acknowledge the assistance of the members of the Cognitive Medical Technology Laboratory for their feedback on practice presentations and help with lab equipment. I would like to thank Jesse d'Almeida for all the time he put into helping me with my thesis when he had his own to worry about. He spent a lot of late nights and early mornings providing me with feedback, and he was always there pushing me to do my best. I also wish to thank Jade Arruda for her constant encouragement and patience throughout this thesis. Finally, thank you to my family for their love and support throughout my life.

TABLE OF CONTENTS

LIST OF TABLES

LIST OF FIGURES

FIGURE **Page**

CHAPTER 1

INTRODUCTION

The use of robots is becoming increasingly prevalent in medicine and surgery. Worldwide, the number of surgical procedures performed annually with the assistance of robots is estimated to be in excess of 1.2 million [5]. The introduction of robotic technology in the operating room has enabled numerous new minimally invasive surgical techniques. Benefits of robot-assisted minimally invasive surgery include reduced patient discomfort, costs, and hospital time. Robots offer increased precision and enhanced ergonomics. The Da Vinci family of robots (Intuitive Surgical, Sunnyvale, CA) is arguably the most commercially successful class of surgical robots to date. The Da Vinci is a teleoperated robot system that allows the surgeon to manipulate a 3-D vision system and wristed laparoscopic surgical instruments [1].

As the benefits of the synergy between robotics and surgery become increasingly apparent, new application areas continue to materialize. The current frontier in robot-assisted surgery is in the development of flexible robotic arms that can navigate through, and offer dexterity within, confined cavities within the human body. Until recently, commercially available surgical robots did not exhibit these properties: in fact, for the most part, they consist of systems that use traditional, rigid manipulator arms. These manipulators possess a limited number of degrees of freedom, which is simply determined by their number of joints.

The work described in this thesis is rooted in the field of continuum robotics. Continuum (i.e., continuously flexible) robots are a new class of manipulators that can assume (virtually) any curvilinear shape in space. Unlike traditional hyper-redundant manipulators, continuum robots do not use any traditional linkages and therefore they can be easily miniaturized (Fig. 1.1).

Thanks to their small size and flexibility, continuum surgical robots have found application in numerous medical specialties (Fig. 1.2). A review of all the clinical applications of continuum robots is beyond the scope of this thesis, and interested readers are referred to [1].

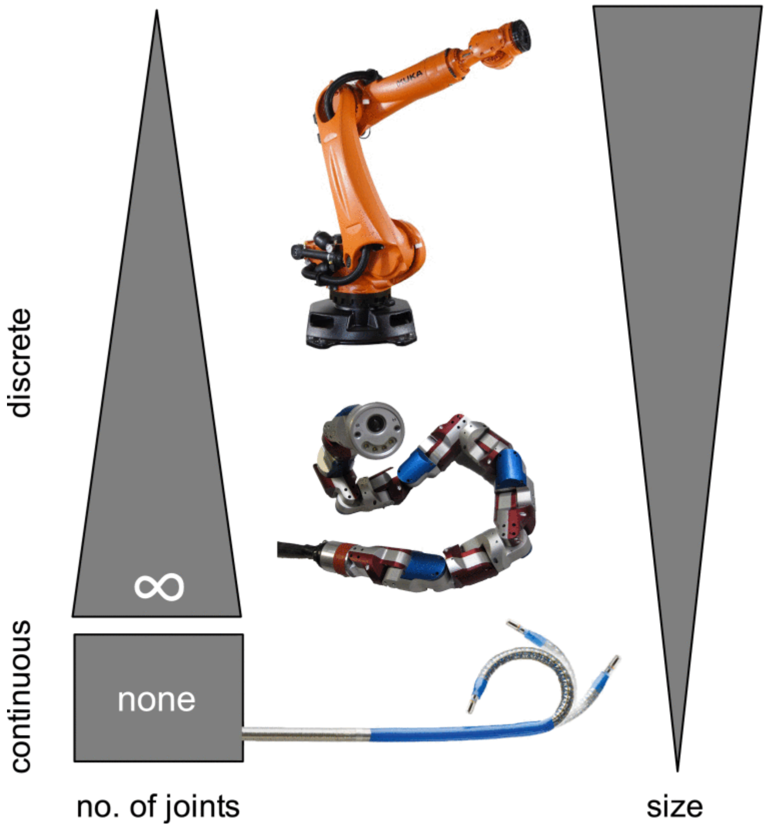

Figure 1.1: *Continuum robots contain no joints but an infinite-Degree-of-Freedom curvilinear elastic structure. Traditional manipulators, in contrast, have discrete links. Reproduced from [1].*

1.1 Notched-Tube Continuum Wrists

Within the field of continuum robots, the problem of creating distal dexterity has recently received a considerable amount of attention. In this thesis, we focus on notched-tube wrists, a class of bending mechanisms fabricated by cutting a pattern of notches into the body of a thin-walled superelastic Nickel-Titanium (Nitinol) tube (Fig. 1.4). Removing material from the body of the tube creates a compliant section that can be articulated by applying a bending moment, e.g., by pulling one or more tendons attached to the tip of the tube. Numerous wrist designs have been proposed in the literature in the past decade, with tube diameters ranging between 0.5 and 10 mm (see e.g. [6, 7, 8, 2, 9, 10, 11, 12, 13, 14, 15]).

Among these, York and Swaney et al. [9, 2] proposed a notched-tube wrist where the notches are created asymmetrically with respect to the centerline of the tube, as shown in Fig. 1.3. Compared to other wrist designs, this solution has two main benefits: (*i*) cutting asymmetric notches effectively offsets the neutral bending plane of the tube, enabling bending in tighter radii; (*ii*) actuation only requires a single tendon, which makes the wrist simple to operate. A downside of asymmetric notches is that they only permit bending in a single direction, but this limitation can be overcome by axially rotating the entire tube. Since their appearance in [9],

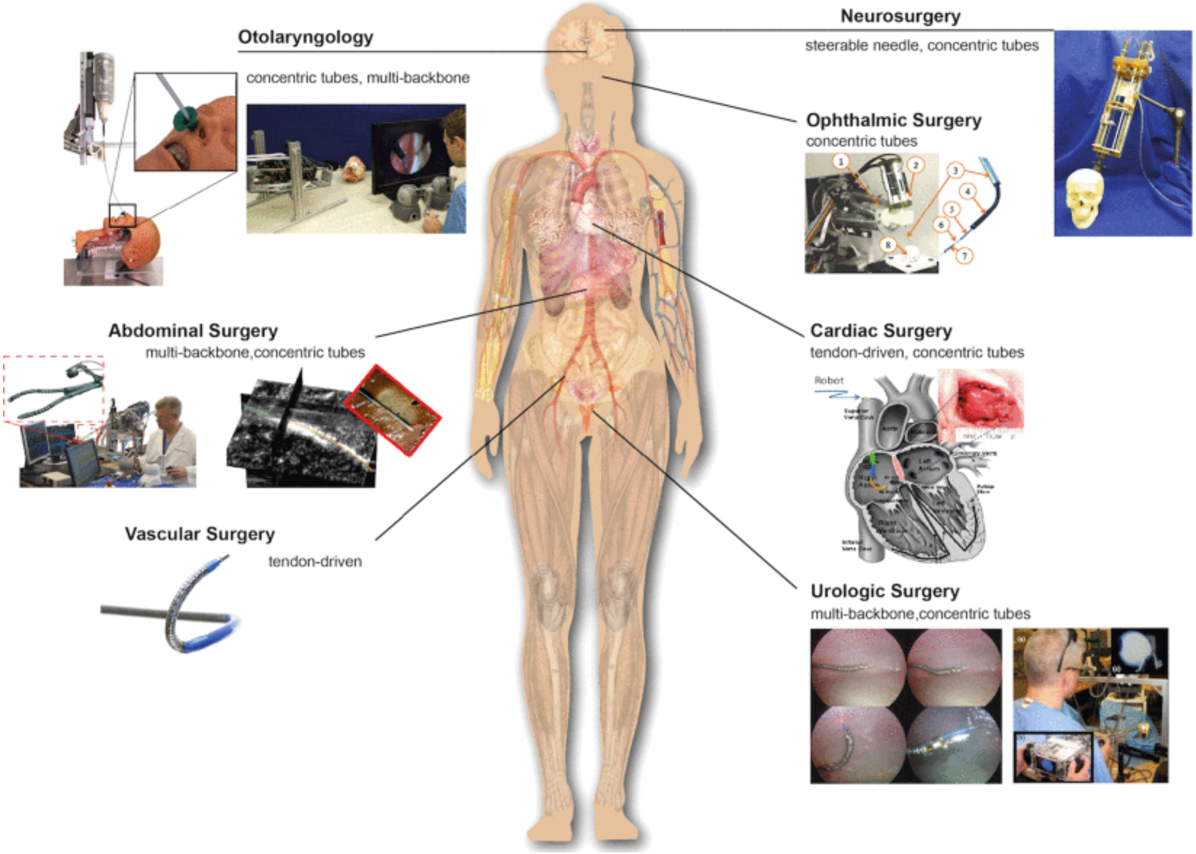

Figure 1.2: *Surgical applications of continuum robots by discipline. Reproduced from [1].*

Figure 1.3: *An example of notched-tube continuum wrist. These mechanisms are manufactured out of a tube of superelastic Nickel-Titanium (Nitinol) and are articulated by pulling a tendon attached to the tip. Notched-tube wrists can be created in small diameters and can bend in tight radii of curvature. A bending radius of 1.42 mm was demonstrated in [2].*

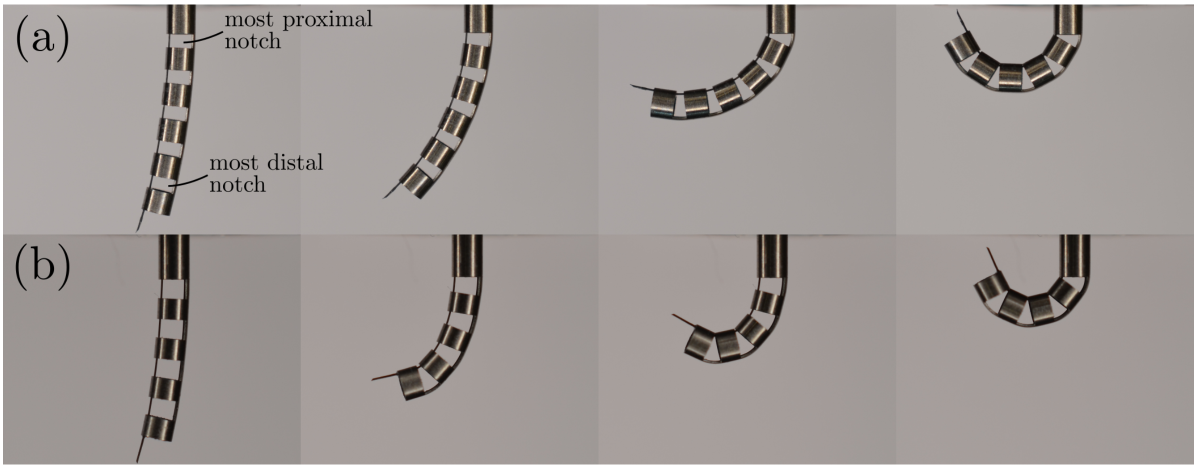

Figure 1.4: *Actuation of two different notched-tube wrists. In wrist (a), which features five identical notches, the most proximal notch bends first (due to tendon friction, which makes the moment highest at the base of the device), while the most distal notch is the last one to reach the hard stop. Wrist (b), which features variable notch depths with the tip notch being deepest, exhibits the opposite behavior, i.e., the most distal notch is the one that closes first since it is the least stiff of the notches (tip-first bending). In this thesis, we propose a mechanics model capable of explaining these different behaviors.*

asymmetric notched-tube wrists have rapidly been adopted in the development of numerous medical devices, including instruments for endoscopic ear procedures [16, 17, 18, 19], hand-held tools for brain surgery [20], a set of miniaturized instruments for the Da Vinci robot [21, 22], a robotic radiofrequency (RF) probe for the treatment of liver tumors [23], and a pair of forceps for robot-assisted vocal folds surgery [24].

While asymmetric notched-tube wrists are conceptually simple to manufacture and operate, their mechanics have previously been modeled using the assumptions that the tendon is frictionless and the material is linear elastic. In this thesis, we relax these assumptions in order to describe the non-constant curvature shapes that these devices can sometimes take on.

Initial kinematic models (without friction and material nonlinearities) of notched-tube wrists predict constant curvature shapes (see [3] for an overview of the kinematics of constant curvature continuum robots). While a constant curvature model is convenient and can work in some applications, one can observe practical devices taking on variable curvature shapes (see Fig. 1.4). To accurately model wrist deflection, it is necessary to understand how friction and material nonlinearities change the loading conditions applied by the tendon at each notch.

To accomplish this, in this thesis we formulate a mechanics-based model that incorporates friction and material nonlinearities to describe the deflection of each individual notch. We model frictional losses along the tendon using the capstan friction model, producing a system of nonlinear equations that can be solved iteratively to calculate the bending moment experienced by each individual notch, and hence the corresponding deflection. Experiments demonstrate the descriptive power of the proposed model. We compare the importance of accounting for friction and material nonlinearities by comparing our model to versions of our model with assumptions made in prior literature, namely one where we assume linear material properties but still account for friction; one where we assume linear material properties and consider the tendon to be frictionless; and one where we assume nonlinear material properties and consider the tendon to be frictionless. The models without friction maintain constant curvature among the notches while the models with friction predict each notch will have a variable curvature.

1.2 Scope of Thesis

The main contributions of this thesis are:

1. A model for tendon friction in asymmetric notched joints. We add a capstan friction term that models the reduced local moment experienced by each notch. Applying Castigliano's Second Theorem, we can determine the angular deflection of the individual notches based on the local moment experienced.
2. A technique to approximate the nonlinear stress-strain curve of Nitinol. We obtain a local linearized approximation of the material modulus, suitable for use in the deflection model.

1.3 Outline

The remaining four chapters of the thesis are organized in the following manner:

Chapter 2 presents an overview of the current modeling techniques used for continuum robots. Specific focus is given to modeling techniques currently used for asymmetric notched-tube wrists. Both kinematic and static models for these wrists are reviewed.

Chapter 3 presents a novel approach to model the angular deflection of the asymmetric notched-tube wrist assuming tendon friction and material nonlinearities.

Chapter 4 presents the experimental verification of the model. We compare the model to experimental data from three uniquely constructed wrists.

Chapter 5 concludes the thesis and discusses the limitations as well as uses of the model.

CHAPTER 2

BACKGROUND: KINEMATICS AND STATICS OF NOTCHED-TUBE CONTINUUM WRISTS

In this chapter, we introduce the mathematical framework necessary to model the mechanics of notched-tube continuum wrists. We begin with a review of the continuum robot kinematics developed by Webster et. al. [3]. We then delve into existing kinematics and statics models for notched-tube wrists developed in prior literature which provides a foundation for the mechanics model proposed in this thesis.

2.1 Kinematics of Continuum Robots

In prior work, Webster et al. [3] established a unified framework to model the kinematics of continuum robots. By modeling continuum robots as constant curvature links, the kinematics can be separated into a robot-independent and robot-dependent mapping. While the work of this thesis focuses on the robot-dependent kinematics of notched wrists, we present the full framework below.

The key modeling assumption of this framework is that continuum robots bend in a shape that can be described as a sequence of piecewise constant curvature segments (which in the following we shall refer to as “links"), each of which can be described by a set of arc parameters. The arc parameters for a single continuum link are illustrated in Fig. 2.1: they are, namely, the curvature κ, the rotation ϕ, and the arc length s. Having established this new vector space that describes the geometry of continuum links, the forward kinematics of continuum robots can then be modeled as a two-step process, as illustrated in Fig. 2.2: a *robot-independent* mapping between the arc parameters space and the task space; and a *robot-dependent* mapping between the configuration space of the robot (i.e., the set all of all possible actuator values $\mathbf{q} \in \mathbb{R}^n$, where n

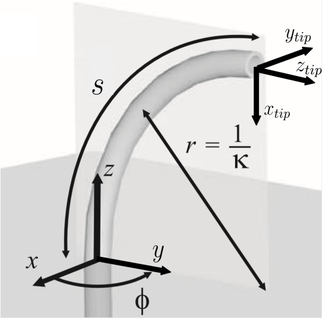

Figure 2.1: *The arc parameters, κ, φ, and s, for a constant curvature segment. The curvature of the arc is κ. The base rotation is φ. The arc length of the tube is s. Adapted from [3].*

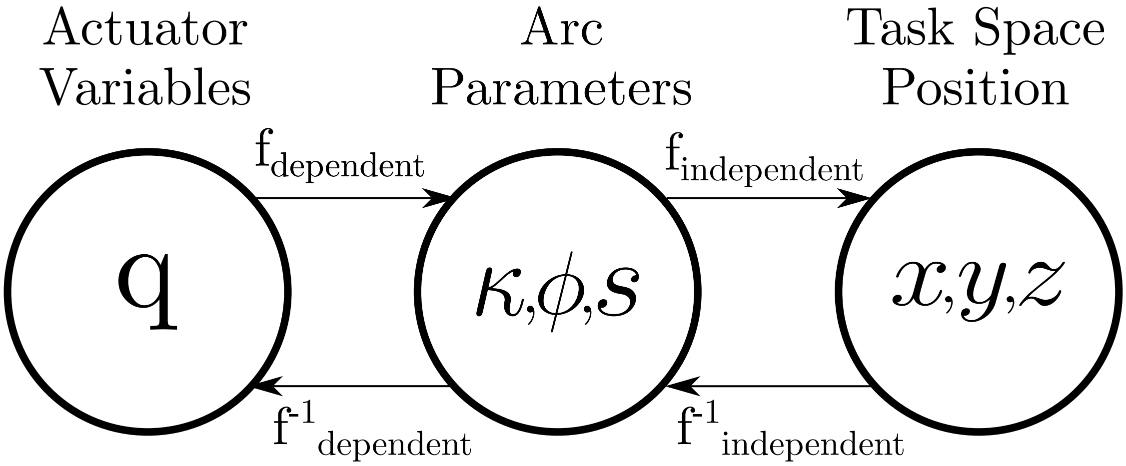

Figure 2.2: *To determine the tip position of the end effector, the actuator variables are first mapped to a set of arc parameters (curvature, rotation, and arc length). The arc parameters are then mapped to a tip position in Cartesian Coordinates [3].*

is the number of degrees of freedom of the robot) and the arc parameters space. In the following, we analyze each of these mappings in more detail.

2.1.1 Robot Independent Kinematics

For a single curved link (see Fig. 2.1), the transformation between the base of the link to the tip can calculated using the following product of exponentials:

$$T = e^{\hat{\xi}_{rot}\phi} e^{\hat{\xi}_{inp} s} \tag{2.1}$$

where ξ_{rot} and ξ_{inp} are two 6-dimensional twist vectors. The first twist, ξ_{rot}, is a screw axis representing a rotation about the z-axis of the link, i.e.,

$$\xi_{rot} = \begin{bmatrix} v_{rot} \\ w_{rot} \end{bmatrix} = \begin{bmatrix} 0 & 0 & 0 & 0 & 0 & 1 \end{bmatrix}^T \tag{2.2}$$

The second twist, ξ_{inp}, represents an in-plane transformation which translates the coordinate frame along the link from base to tip given a specific curvature κ, i.e.,

$$\xi_{inp} = \begin{bmatrix} v_{inp} \\ w_{inp} \end{bmatrix} = \begin{bmatrix} 0 & 0 & 1 & 0 & \kappa & 0 \end{bmatrix}^T \tag{2.3}$$

To calculate the robot-independent transformation matrix for each curved section, we take the twist coordinates above and map them to 4×4 elements of $\mathfrak{se}(3)$ (i.e., the Lie Algebra of the special Euclidean group SE(3)):

$$\hat{\xi}_{rot} = \begin{bmatrix} \hat{\omega}_{rot} & v_{rot} \\ 0 & 0 \end{bmatrix} = \begin{bmatrix} 0 & -1 & 0 & 0 \\ 1 & 0 & 0 & 0 \\ 0 & 0 & 0 & 0 \\ 0 & 0 & 0 & 0 \end{bmatrix} \tag{2.4}$$

$$\hat{\xi}_{inp} = \begin{bmatrix} \hat{\omega}_{inp} & v_{inp} \\ 0 & 0 \end{bmatrix} = \begin{bmatrix} 0 & 0 & \kappa & 0 \\ 0 & 0 & 0 & 0 \\ -\kappa & 0 & 0 & 1 \\ 0 & 0 & 0 & 0 \end{bmatrix} \tag{2.5}$$

We recognize that $\mathfrak{se}(3)$ can be parameterized by an element in $\mathbb{R}^6$, so we define the $\hat{\cdot}$ operator to represent the isomorphic mapping from $\mathbb{R}^6$ to $\mathfrak{se}(3)$ [25]. Therefore, for $\xi = [v_x\ v_y\ v_z\ u_x\ u_y\ u_z]^T \in \mathbb{R}^6$:

$$\hat{\xi} = \begin{bmatrix} 0 & -u_z & u_y & v_x \\ u_z & 0 & -u_x & v_y \\ -u_y & u_x & 0 & v_z \\ 0 & 0 & 0 & 0 \end{bmatrix} \tag{2.6}$$

Similarly, we recognize $\mathfrak{so}(3)$ is a 3×3 skew-symmetric matrix which is isomorphic in $\mathbb{R}^3$. We overload the $\hat{\cdot}$ operator to map vectors in $\mathbb{R}^3$ to $\mathfrak{so}(3)$ as follows [25]. For $u = [u_x\ u_y\ u_z]^T \in \mathbb{R}^3$:

$$\hat{u} = \begin{bmatrix} 0 & -u_z & u_y \\ u_z & 0 & -u_x \\ -u_y & u_x & 0 \end{bmatrix} \tag{2.7}$$

Then, expanding Eq. 2.1 produces the following transformation matrix:

$$T = \begin{bmatrix} \cos(\phi)\cos(\kappa s) & -\sin(\phi) & \cos(\phi)\sin(\kappa s) & \frac{\cos(\phi)(1-\cos(\kappa s))}{\kappa} \\ \sin(\phi)\cos(\kappa s) & \cos(\phi) & \sin(\phi)\sin(\kappa s) & \frac{\sin(\phi)(1-\cos(\kappa s))}{\kappa} \\ -\sin(\kappa s) & 0 & \cos(\kappa s) & \frac{\sin(\kappa s)}{\kappa} \\ 0 & 0 & 0 & 1 \end{bmatrix} \tag{2.8}$$

As we shall see in the following, the transformation matrix in Eq. 2.8 can be directly applied to model the kinematics of individual curved sections in a robot [2]. Creating a transformation matrix for each section of the robot and multiplying them sequentially will produce the transformation from the base of the robot to the tip.

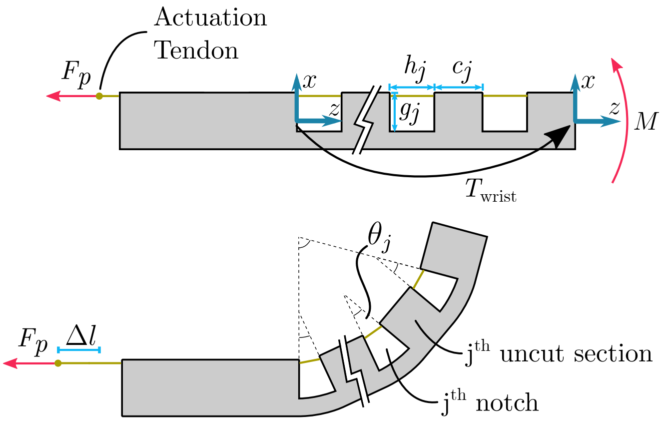

Figure 2.3: *A notched-tube wrist is an open kinematic chain consisting of a sequence of interleaving notches and uncut sections. Throughout this thesis, we use* c_j *to indicate the length of the* j^{th} *uncut section, while* h_j *and* g_j *respectively denote the length and depth of the* j^{th} *notch. Wrist actuation is performed by applying a pulling force* F_p *on the tendon. Kinematic models provide a mapping between the tendon displacement* Δl *and the tube pose* $T_{wrist} \in SE(3)$*. A consequence of assuming a frictionless tendon in prior models is that each notch undergoes the same amount of deflection* θ_j*.*

2.1.2 Robot-Dependent Kinematics

The purpose of the robot-dependent kinematics is to create a relationship between the actuator variables of the robot and the arc parameters of the curved links. While the equations in Section 2.1.1 hold for any piecewise constant curvature robot, there is no single closed-form solution to the robot-dependent kinematics. The design of the robot will dictate how to map the actuator variables to the arc parameters. As we shall see later in this chapter, this is the case of notched-tube wrists, whose robot-dependent kinematic relations are presented in Section 2.2.1.

2.2 Prior Modeling of Asymmetric Notched-Tube Wrists

Let us consider a generic notched-tube wrist, with dimensions as noted in Fig. 2.3. Throughout this thesis, we will use the convention of numbering notches from 1 (most proximal) to n (most distal). When a pulling force F_p is applied on the actuation tendon, a moment M will be created at the tip of the tube, which will make the wrist bend. We make several key modeling assumptions about the tendon: it is attached to the tip of the tube, on the opposite side of the wrist spine, it is inextensible, and it will not significantly contribute to the flexural compliance of the wrist.

2.2.1 Wrist Kinematics

York and Swaney et. al. previously developed a geometric robot-dependent forward kinematics model. The model determines the arc parameters κ and s based on the tendon displacement

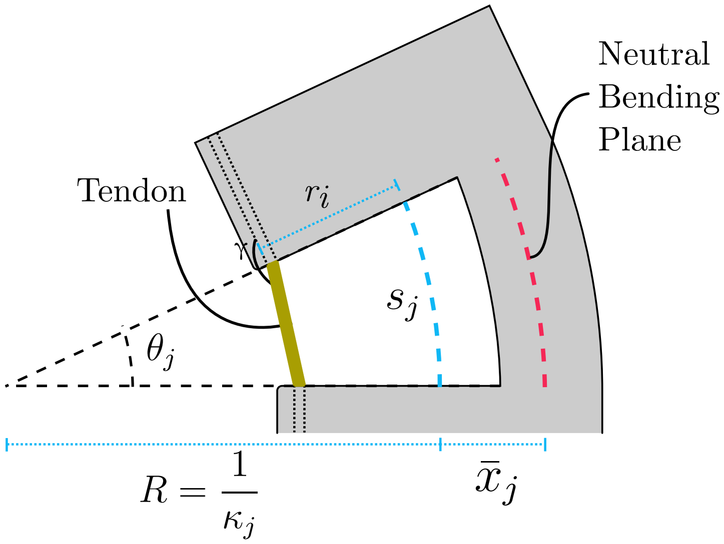

Figure 2.4: *Representation of a single notch and the arc parameters κ_j and s_j that describe it. The neutral bending plane maintains the length h_j, the height of the cut, during bending. The distance of the neutral bending plane from the center of the tube is denoted by $\bar{x}_j$. Reproduced from [2].*

Δl. To simplify the analysis, the authors assume a frictionless tendon, and only model a single notched section - with the assumption that all notches in the wrist undergo the same deflection.

Let us consider an individual notched section (Figure 2.4) which we assume is bending in a constant curvature arc. We begin by calculating the distance between the neutral bending plane and the centerline of the tube. The neutral bending plane is the area of the tube that does not experience longitudinal strain when bent and is located at the centroid of the notch's horizontal cross-section. For the sake of conciseness, the calculation of $\bar{x}_j$ is omitted here, and interested readers are referred to Appendix A. We can use $\bar{x}_j$ and the notch height, h_j, to find the mapping from curvature, κ_j, to tendon displacement, Δl, using the chord function and arc geometry [9]:

$$\Delta l = h_j - 2\left(\frac{1}{\kappa_j} - r_i\right)\sin\left(\frac{\kappa_j h_j}{2(1+\bar{x}_j\kappa_j)}\right). \tag{2.9}$$

Then by applying a small angle approximation, we can invert Eq. 2.9 to define curvature as a function of tendon displacement:

$$\kappa_j \approx \frac{\Delta l}{h_j(r_i+\bar{x}_j) - \Delta l \bar{x}_j}. \tag{2.10}$$

Once κ_j is known, the arc length s_j and the bending angle θ_j can be found using arc geometry:

$$s_j = \frac{h_j}{1+\bar{x}_j\kappa_j}, \tag{2.11}$$

$$\theta_j = \kappa_j s_j. \tag{2.12}$$

The relations above permit the calculation of the arc parameters κ_j and s_j given the amount of tendon displacement Δl. Then using the transformation matrices from Eq. 2.8 we can build the forward kinematics for a notched tube wrist [3]:

$$T_{\text{wrist}} = \prod_{j=1}^{n} T_{\text{notch},j}\, T_{\text{uncut},j} \tag{2.13}$$

here $T_{\text{notch},j}$ and $T_{\text{uncut},j}$ are the transformations across the j^{th} notched and uncut sections, respectively. We assume that uncut sections do not bend, therefore $T_{\text{uncut},j}$ is a simple translation along the z axis by a distance c_j equal to the length of the j^{th} uncut section. For the notched sections, $T_{\text{notch},j}$ can be calculate using Eq. 2.8 where the curvature and arc length are calculated with Eq. 2.10 and Eq. 2.11.

The assumption of a frictionless tendon in prior kinematic modeling implies that during actuation, for a wrist comprised of n geometrically identical notches, each notch undergoes the same amount of deflection, i.e., $\theta_1 = \theta_2 = \cdots = \theta_n$. As we have shown earlier in Fig. 1.4, this assumption does not always describe the shape of these devices accurately. As we shall see later in Chapter 3, we relax this assumption and explicitly model tendon friction and material nonlinearities to describe these non-constant curvature behaviors.

2.2.2 Wrist Statics

In [2], York and Swaney also propose a statics model to determine the actuation force necessary for wrist actuation. Briefly, the authors first calculate the total amount of elastic energy U stored in the wrist, then apply Castigliano's First Theorem to calculate the bending Moment M acting on the wrist. The authors maintain their assumption that each notch bends in a constant curvature arc. Based on this assumption, the strain along the length of the wrist varies proportionally to the distance from the neutral bending plane:

$$\varepsilon = \frac{\kappa(y - \bar{x})}{1 + \bar{x}\kappa} \tag{2.14}$$

where y is the distance between the neutral bending plane and location of interest in the backbone [2].

The strain energy in the system can then be computed using the relationship between the geometry and the material deformation. The behavior of Nitinol is highly non-linear, though, and the authors simplify the stress-strain relationship with the following piecewise equation:

$$\sigma(\varepsilon) = \begin{cases} \sigma_{lp} & \varepsilon \leq \frac{\sigma_{lp}}{E} \\ E\varepsilon & \frac{\sigma_{lp}}{E} < \varepsilon \leq \frac{\sigma_{up}}{E} \\ \sigma_{up} & \frac{\sigma_{up}}{E} < \varepsilon \end{cases} \tag{2.15}$$

where E is the elastic modulus of the material, σ_{lp} is the lower stress plateau, and σ_{up} is the upper stress plateau.

The strain energy density, $W(\varepsilon)$, is the area under the stress-strain curve and is defined by the integral:

$$W(\varepsilon) = \int_0^{\varepsilon} \sigma(e)de. \tag{2.16}$$

The integral of the strain energy density of a notch with respect to the volume of the notch is the strain energy. The total strain energy, $U(\kappa)$, stored in the wrist is given by the strain energy in a single notch multiplied by the number of notches:

$$U(\kappa) = n\int_{V_c} W(\varepsilon(y,\kappa))dV \tag{2.17}$$

where V_c is the volume of the notched section. The relationship between the tip deflection, θ, and the input force F is given by Castigliano's first theorem:

$$\frac{\partial U}{\partial \theta} = M = Fd \tag{2.18}$$

where d is the length of the moment arm given by $d = (r_i + \bar{x})$ [2]. The authors include a frictional component strictly to measure the increase in actuation force necessary to bend the tube. The frictional force does not have any effect on the modeled notch closure sequence and is not used to measure the different local moments experienced by the notches. The frictional force is applied at the corners of the notched sections and is described as:

$$F = \eta F_{tendon} = \frac{sin(\gamma/2) - \mu_s \cos(\gamma/2)}{sin(\gamma/2) + \mu_s \cos(\gamma/2)} \tag{2.19}$$

where γ is the angle defined in Figure 2.4 and μ_s is the coefficient of friction between the tendon and the tube. Solving Eq. 2.18 for the force of the tendon we get:

$$F_{tendon} = \frac{1}{\eta^{2n}L}\frac{\partial U(\kappa)}{\partial \theta}. \tag{2.20}$$

In separate work, Eastwood *et al.* [4] developed a kineto-static model that uses Castigliano's Second Theorem to estimate the deflection of a wrist subject to external forces.

The authors first model the second moment of area for the beam $I(z)$, which is a discontinuous function because of the removed material from the tube. The second moment of area is a function of the tube's length:

$$I(z) = \begin{cases} \pi(r_o^2 - r_i^2)/4 & if(0 < z \leq a) \\ I_{II} & if(a < z < L-b) \\ \pi(r_o^2 - r_i^2)/4 & if(L-b < z) \leq L \end{cases} \tag{2.21}$$

where the position along the beam, $z \in [0,L]$, is described by Fig 2.5. The function I_{II} represents the second moment of area for the notched section of the tube and is itself a piecewise function. For a cut section of the tube, the second moment of area is the superposition of the second moment of area for two circular segments, $\tilde{I}_{II}$. One circular segment uses the inner radius of the tube and

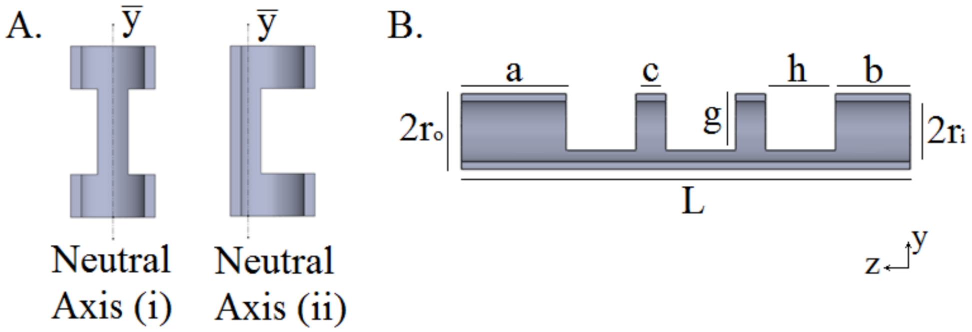

Figure 2.5: *The representation of the neutral bending plane and notched-tube parameters used in [4]. Here a represents the length of the tube before the first notch and b is the length after the last notch. Reproduced from [4].*

one uses the outer radius. For an uncut section, the second moment of area is just the second moment of area for a cylinder.

$$I_{II} = \begin{cases} \pi(r_o^4 - r_i^4)/4 & if(z-b)Mod(h+c) < c \\ \tilde{I}_{II} - \bar{y}^2(A_s(r_o,q_o) - A_s(r_i,q_i)) & otherwise \end{cases} \tag{2.22}$$

In Eq. 2.22, $A_s(r,q)$ is the area of the circular segment with radius r, and angle q.

The authors apply Castigliano's second theorem to calculate the deflection of a point on the notched-wrist where a load is applied. Since they are assuming a load is applied to the tip of the tube, to determine the deflection of other areas on the notched-wrist, a dummy load is applied at the point of interest. The strain energy of the system is given by the following equation:

$$U(z) = \int_0^L \frac{M^2}{2EI} dz. \tag{2.23}$$

The authors then calculate the deflection of the points on the beam by applying Castigliano's 2nd Theorem:

$$\Delta y = \frac{\partial U(z)}{\partial Q}. \tag{2.24}$$

Here it is important to note that the authors are concerned with external loads being applied to the tube. They are not measuring the impact the internal forces created by the wire will have on the deflection of the tube which is instead the main focus of the work described in this thesis.

2.3 Limitations of Current Models

The kinematic model we discussed assumes a frictionless tendon, and so each notch, when the tube is actuated, will experience the same tendon displacement and bend the same amount. As we have seen though, (see Fig 1.4), when the tube is actuated, each notch has a different bending rate. In some cases, we see the proximal notches closing more quickly and in others we

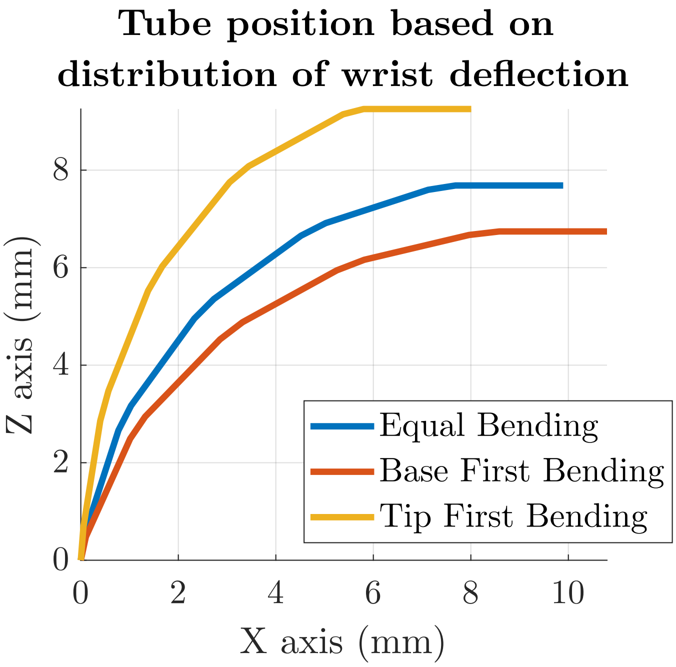

Figure 2.6: *If we change the distribution of the wrist deflection among the notches, we can get drastically different tube shapes. in this image, each tube bends a total of 90 degrees but the distribution of the bending angle varies among the tubes: the blue line has an equal bending distribution among the notches, the red line has the proximal notches take a majority of the total deflection, and the yellow line has the distal notches take a majority of the total deflection. The current models assume that we have an equal bending distribution (blue line), but this is not the case. Continuing to use the assumption that each notch bends the same amount can produce large inaccuracies in the tip position of the tube.*

see the distal notches closing more quickly. This assumption, while it simplifies the calculations, can create large inaccuracies when determining the position of the tube as seen in Fig. 2.6. Similarly, the statics model developed by Swaney et al. maintained the assumption that each notch would bend uniformly. The friction term was included purely to model the necessary increase in actuation force, but not to model the individual notch bending rates and so suffers from the same inaccuracies as the kinematic model. The statics model developed by Eastwood et al. is mainly concerned with external forces applied to the tube, and so does not model the internal forces between the tendon and tube. Additionally, this model assumes a purely elastic material and does not account for the material nonlinearities of Nitinol. As we shall see in the following chapter, we believe it is the frictional forces between the tendon and the tube, as well as the material nonlinearities, that contribute to the unique notch deflection rates, we see in the tubes.

CHAPTER 3

WRIST MECHANICS

We now study the mechanics of notched tube wrists, and formulate a model that describes the deflection of each individual notch. Our analysis is structured as follows: we first focus on the mechanics of notched sections and use Castigliano's Second Theorem to derive a formulation for the notch deflection based on the local bending moment experienced at each notch. We then propose a model for the frictional forces occurring between the actuation tendon and the walls of the tube, and study how these losses affect the local moments. The result of our analysis is a set of recursive equations that can be solved to calculate the wrist kinematics.

3.1 Force Model

Throughout our analysis, we consider the same generic notched wrist illustrated earlier in Fig. 2.3. To denote the wrist dimensions, we use the nomenclature introduced in Section 2.2. For convenience, relevant variables are summarized in Table 3.1.

3.1.1 Notch Deflection via Castigliano's Second Theorem

Recall from basic mechanics [26] that the total strain energy U stored in a cantilever beam of length L subject to a bending moment M is given by:

$$U = \int_L \frac{M^2}{2EI} dz \tag{3.1}$$

where E is the elastic modulus, and I is the second moment of area of the beam about its neutral axis. This relation is valid so long as we operate within the linear (elastic) region of the stress-strain curve for the material that the beam is made of. In Section 3.1.3, we will extend

Table 3.1: *Wrist Parameters*

r_i	Inner Radius of Wrist
h_j	Height of notch
c_j	Length of uncut section
g_j	Depth of cut for notch
θ_j	Angle of notch deflection
$\bar{x}_j$	Distance to neutral bending plane
n	Number of notches

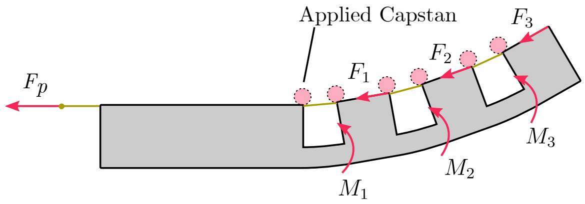

Figure 3.1: *Diagram of the forces and moments being experienced at each notch due to the tendon force and the capstan loss model being applied at each cut section of tube.*

our analysis to consider the case of materials with a non-linear stress-strain curve, as is the case with Nitinol.

If we assume that M, E, and I are uniform along the length of the beam, Eq. 3.1 simplifies to:

$$U = \frac{M^2 L}{2EI}. \tag{3.2}$$

Having obtained a relation for the strain energy U, we can now use Castigliano's Second Theorem to determine the angular deflection of the beam:

$$\theta = \frac{\partial U}{\partial M} = \frac{ML}{EI}. \tag{3.3}$$

These results for a cantilever beam can be applied to calculate the deflection of each notched section in a wrist. For a notched-tube joint with n notches, the bending angle of the j^{th} notch θ_j is given by:

$$\theta_j = \frac{M_j h_j}{E_j I_j} \tag{3.4}$$

where M_j is the local bending moment, E_j is the local elastic modulus, I_j is the second moment of area, and h_j is the notch height. Note that this equation is general in the sense that it allows for variations in notch geometry and material.

3.1.2 Modeling the Frictional Losses on the Actuation Tendon

We now study tendon friction and evaluate how it affects the loading conditions at each notch. Without loss of generality, let us consider the 3-notch wrist shown in Fig. 3.1. Pulling on the

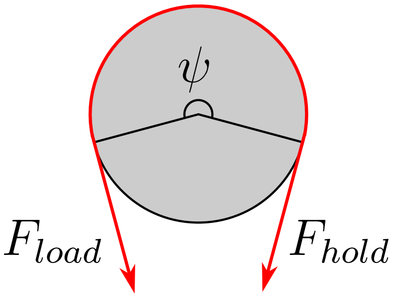

Figure 3.2: *Due to the tension on the tendon and frictional forces between the tendon and the capstan surface about the angle ψ, a small holding force can hold a much higher loading force.*

tendon with a force F_p exerts a force F_3 at the distal tip of the wrist. If there were no losses, then F_p would be equal to F_3. However, as it was discovered in [9, 2], F_3 will generally be smaller than F_p due to the frictional contact between the tendon and the corners of the notched sections. As the tendon is pulled to deflect the wrist from an initially straight configuration, friction will progressively reduce the tension on the tendon towards the distal end of the wrist. We propose to model these interactions using a capstan loss model. For a tendon or rope wrapped around an object, the loading force gets reduced by an exponential term relative to the angle, ψ and the coefficient of friction μ. The application of an ideal capstan is demonstrated in Fig. 3.2 and by the following equation:

$$F_{load}e^{-\mu\psi} = F_{hold}. \tag{3.5}$$

The capstan is applied at the corners of each notch, denoted with a pink circle in Fig. 3.1. The tendon travels around each capstan with an angle of $\frac{\theta_j}{2}$. As the tendon passes through a notched section it will pass around two capstans and will experience the equivalent frictional loss of a single capstan about an angle of θ_j. Therefore we can model the force experienced at each notch, F_j, as a function of the pulling force, F_p and the angle of each notch.

$$F_j = F_p \prod_{k=1}^{j} e^{-\mu\theta_k}. \tag{3.6}$$

We are now ready to calculate the bending moment experienced by each notch, which is simply given by:

$$M_j = F_j(r_i + \bar{x}_j). \tag{3.7}$$

In the equation above, the term $r_i + \bar{x}_j$ represents the moment arm. Recall from Section 2.2.2 that this expression for the moment arm length is valid so long the actuation tendon is attached at the tip of the tube on the opposite side of the spine

Finally, we can substitute M_j in Eq. (3.4) to obtain an expression that relates the bending angle of the j$^{\text{th}}$ notch to the pulling force F_p, yielding the key modeling result of this thesis:

$$\theta_j = \frac{(r_i + \bar{x}_j)h_j}{E_j I_j} F_{pw} \prod_{k=1}^{j} e^{-\mu\theta_k}. \tag{3.8}$$

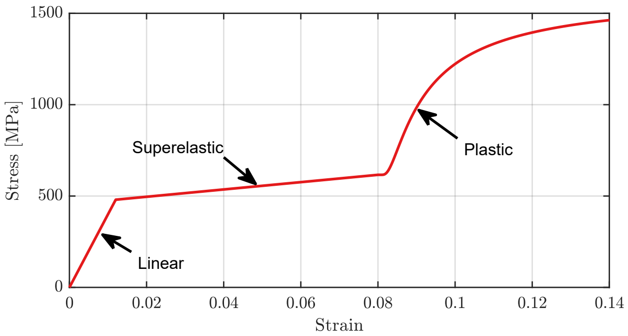

Figure 3.3: *Illustrative stress-strain curve of Nitinol as per Eq.* (3.9).

The system of transcendental equations above - note that θ_j appears both on the left-hand side as a linear term and on the right-hand side as an argument to one of the exponentials - can be solved numerically to obtain the notch deflections for a given actuation force F_p. Note also how the right-hand side of Eq. (3.8) contains E_j, i.e., the elastic modulus of the material. To account for the fact that Nitinol has a nonlinear stress-strain curve, we replace E_j with an *effective* (secant) modulus $E_{\mathrm{eff},j}$, as we describe in the following.

3.1.3 Handling Material Nonlinearities

The stress-strain curve of Nitinol has a distinctive non-linear behavior that is convenient to approximate using a piecewise formulation (adapted and slightly modified from the model discussed in Section 2.2):

$$\sigma(\varepsilon) = \begin{cases} \varepsilon E_{lin} & \varepsilon \le \varepsilon_l \\ \sigma_l + (\varepsilon - \varepsilon_l) E_{se} & \varepsilon_l < \varepsilon \le \varepsilon_p \\ \sigma_p + E_p e^{-\beta/(\varepsilon - \varepsilon_p)} & \varepsilon_p < \varepsilon \end{cases} \tag{3.9}$$

where E_{lin}, E_{se}, and E_p are the effective moduli in the linear, super-elastic, and plastic regions (respectively); σ_l, σ_p are the lower and upper plateau stresses; ε_l, ε_p are the lower and upper plateau strains; and β is a heuristic parameter. An illustrative stress-strain curve of Nitinol, showing these three regions, is shown in Fig. 3.3.

From Eq. 3.9 and Fig. 3.3, it is evident that so long as we operate within the elastic region of the stress-strain curve, it is possible to estimate the deflection θ_j by simply replacing E_j with E_{lin} in Eq. (3.8). However, as soon as the amount of strain created on the notch exceeds ε_l, i.e., as soon as the material enters the superelastic regime, the linear modulus E_{lin} no longer adequately captures the mechanics of the notch, and we need to find an approximation for E_j that ensures consistency with the assumptions of the model. For this purpose, we use the effective (secant) modulus $E_{\mathrm{eff},j}$. To calculate $E_{\mathrm{eff},j}$, we use a gradient descent approach. We begin by setting

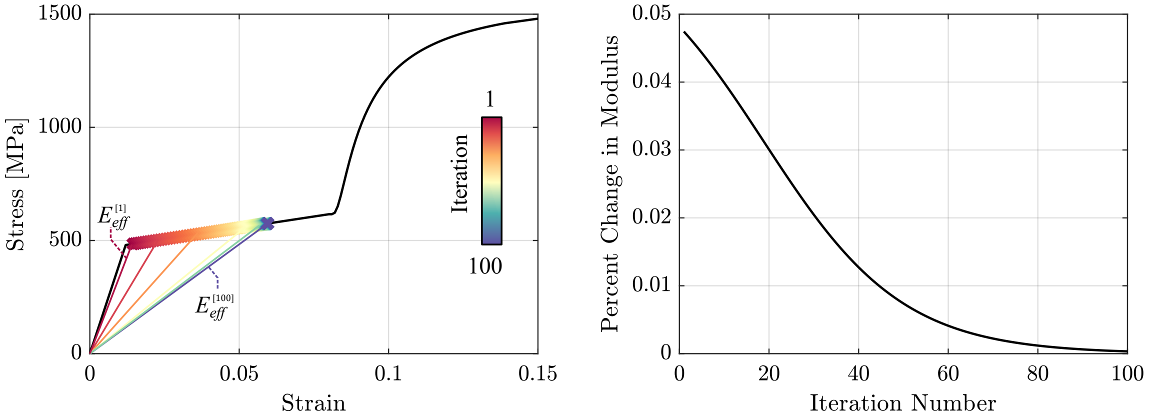

Figure 3.4: *Iterative secant modulus approximation of superelastic material behavior: (top) modulus approximation for a tube in the superelastic range, (bottom) convergence plot.*

$E_{\text{eff},j}^{[0]} = E_{lin}$, and then use the following update law:

$$E_{\text{eff},j}^{[k]} = E_{\text{eff},j}^{[k-1]} - \eta \left(E_{\text{eff},j}^{[k-1]} - \frac{\sigma_j}{\varepsilon_j} \right) \tag{3.10}$$

where η is the descent rate, and σ_j and ε_j respectively are the stress and strain created on the j$^{\text{th}}$ notched section. The execution of the algorithm is illustrated in Fig. 3.4. At each step k of the algorithm, the values of σ_j and ε_j are updated to reflect the update in the effective elastic modulus. To perform these updates, we use the relations derived in [2], which we report below for completeness:

$$\kappa_j = \frac{\theta_j}{h_j - \bar{x}_j \theta_j}, \tag{3.11}$$

$$\varepsilon_j = \frac{\kappa(r_o - \bar{x}_j)}{1 + \bar{x}_j \kappa}. \tag{3.12}$$

The deflection angle θ_j used in the relations above is calculated by evaluating Eq. (3.8) with a modulus value of $E_{\text{eff},j}^{[k-1]}$. This process is repeated until the modulus converges ($E_{\text{eff},j}^{[k]} - E_{\text{eff},j}^{[k-1]} < \epsilon$). The full algorithm can be seen in Appendix B.

CHAPTER 4

EXPERIMENTAL VERIFICATION

Here we describe the experiments that we performed to verify the model proposed in the previous chapter. We created three different wrists designs, with notch geometries as listed in Table 4.1. Nitinol tubing was procured from Johnson Matthey (West Chester, PA, USA), and notches were created by laser cutting. Wrists A and B feature a uniform notch geometry, and they were designed to achieve a maximum deflection of 150°and 90°, respectively. These two wrists were designed to test the main hypothesis of this thesis; namely, that uniform-notched wrists undergo non-constant curvature due to the presence of tendon friction, as illustrated earlier in Fig. 1.3(a) (i.e., proximal notches close first). Wrist C was instead designed to compensate for these frictional losses by having increasingly deeper notches towards the distal end, with the goal of replicating the *tip-first* bending behavior observed previously in Fig. 1.3(b).

4.1 Tendon Attachment

In our model, we assume the tendon is attached to the tip of the tube on the opposite side of the wrist spine. In order to guarantee this positioning, we designed a specific procedure for tendon attachment taking advantage of the tube's bending behavior. The tendon is threaded through the tube while the tube itself is resting on a curved platform. The tendon is then pulled towards the table surface, creating tension and causing the tube to bend slightly. This causes the wire to rest in a position opposite the spine, and super glue can be added to the tip of the tube (Fig. 4.1). After the glue has cured, the tension on the wire is released, excess wire is cut, and the wrist is ready for use.

Table 4.1: *Geometric design parameters of the wrists used for experimental verification. Each wrist has an inner diameter of 1.4 mm and an outer diameter of 1.62 mm.*

	Wrist A	Wrist B	Wrist C
h (mm)	0.8	0.5	1.0
c (mm)	2.2	1.5	1.0
g (mm)	1.4	1.4	[1.36, 1.39, 1.42, 1.45]
n	5	5	4

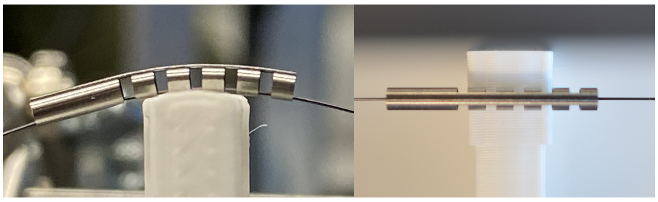

Figure 4.1: *By using a curved surface, the tube bends when tension is applied to the wire. This causes the wire to settle in the ideal position for gluing.*

4.2 Experimental Setup

The experimental setup is shown in Fig. 4.2. Each wrist was mounted on a collet and the actuation tendon was pulled by means of a linear slider (Velmex, Bloomfield, NY, USA). Throughout each experiment, the tension on the tendon was monitored with an FT-17 force sensor (Alberobotics, Genoa, Italy).

Experiments were carried out as follows: starting from an initially straight configuration, each wrist was progressively bent by pulling the tendon in increments of 0.25 mm. At each step, a digital single-lens reflex camera outfitted with a macro objective (Nikkor 40mm f/2.8G, Nikon Corporation, Tokyo, Japan) was used to document wrist deflection. This procedure was repeated five times on each wrist, i.e., each wrist was cycled for a total of five times. After the experiment, each photograph was analyzed with a custom image processing MATLAB script (MathWorks Inc., Natick, MA, USA) to measure the bending angle of each notch.

4.3 Identification of Material Properties

For reasonable (non-plastic) strains, the mechanics model in Eq. (3.8) is dependent on three different material properties of Nitinol, namely the linear elastic modulus E_{lin}, the superelastic modulus E_{se}, and the lower strain plateau ε_{lp}, plus the coefficient of friction μ of the actuation tendon. To identify these parameters, we ran a global optimization routine in MATLAB seeking to solve the following problem:

$$\min_{E_{lin},E_{se},\varepsilon_{lp},\mu} ||e_A|| + ||e_B|| + ||e_C|| \tag{4.1}$$

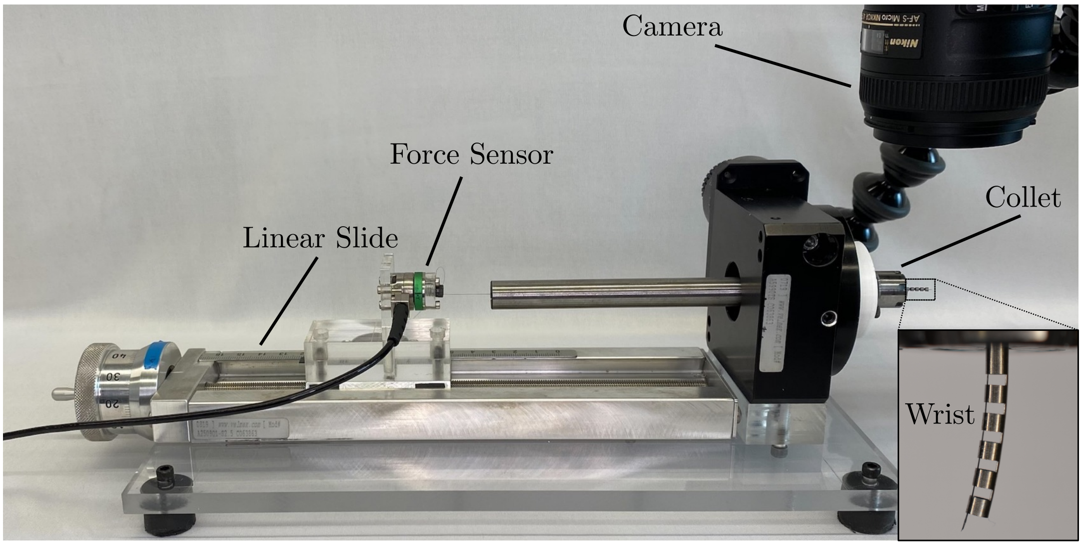

Figure 4.2: *Experimental setup. Notched-tube wrists were mounted in a collet, and a linear slider was used to pull the actuation tendon. Tension on the tendon was measured by means of a force sensor, while the wrist deflection was recorded with a digital single-lens reflex camera.*

Table 4.2: *Material parameters determined by global search optimization.*

E_{lin}	E_{se}	ε_{lp}	μ
10.7 GPa	2.9 GPa	0.0255	0.13

where e_A, e_B, and e_C, are $(n+1)$-dimensional vectors containing the model Root-Mean-Square-Error (RMSE) of the individual notches and total wrist deflection for Wrist A, Wrist B, and Wrist C respectively, and the $||\cdot||$ operator denotes the Euclidean norm. The error vectors for each wrist were generated using the measured angles from the 5 cycles of each wrist, and the models predicted angles for a given set of parameters. The parameters that minimized the error vectors would minimize our objective function, and the results of the material identification routine produced the parameters listed in Table 4.2.

4.4 Model Verification

Using the material properties identified in the previous section, we generated the plots in Figure 4.3, which show a comparison between experimental data and model predictions. The model was found to accurately predict the deflection of each notch, and hence the curvature of each different wrist. The Root-Mean-Square errors (RMSE) of the model with respect to each individual notch are reported in Table 4.3. The largest observed error was 2.27° (notch 1 in wrist C), while the RMSE was around or below 1° for most other notches.

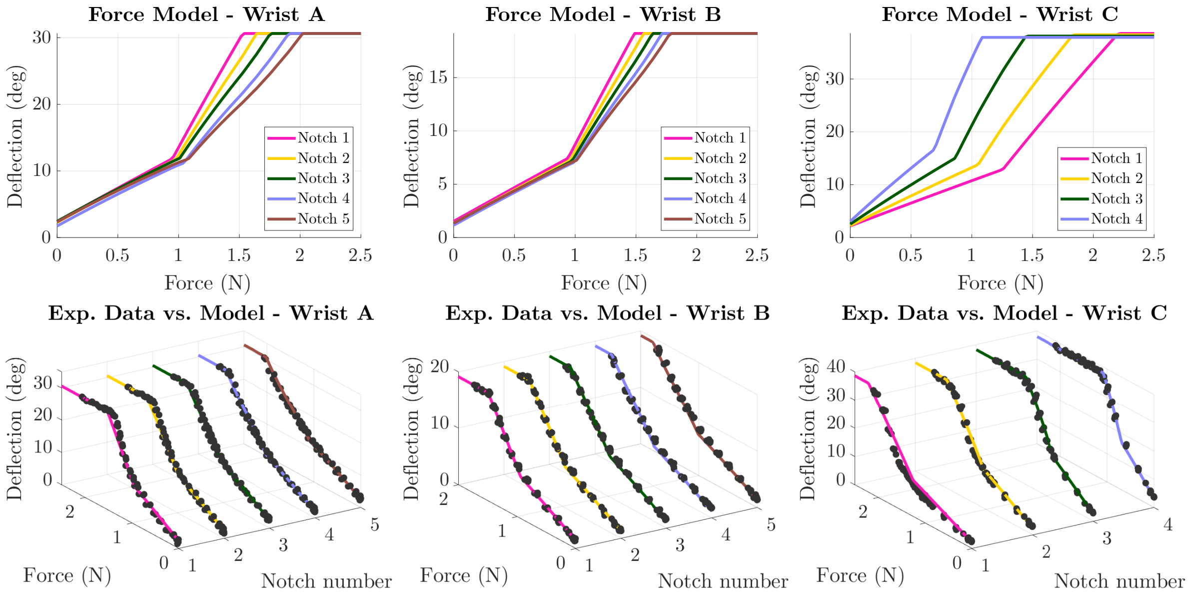

Figure 4.3: *Experimental Results. (Top Row) Model output for the three different wrist designs considered in the experiments. Wrists A and B were designed to exhibit proximal-first bending, while wrist C displayed tip-first bending. Note how the model correctly captures the notch closing sequence in all cases. (Bottom Row) Comparison of model output versus experimental data.*

4.5 Comparison with Simpler Models

To illustrate the importance of accounting for both tendon friction and material nonlinearities, we report results comparing the tracking accuracy of our model against three simpler models, namely one where we assume linear material properties but still account for tendon friction (i.e. Eq. 3.8 assuming $E_j = E_{lin} \forall j$)

$$\theta_j = \frac{(r_i + \bar{x}_j)h_j}{E_{lin} I_j} F_p \prod_{k=1}^{j} e^{-\mu\theta_k}; \tag{4.2}$$

one where we assume linear material properties and consider the tendon to be frictionless (i.e. Eq. 3.8 assuming $E_j = E_{lin} \forall j$ and $\mu = 0$)

$$\theta_j = \frac{(r_i + \bar{x}_j)h_j}{E_{lin} I_j} F_p; \tag{4.3}$$

one where we assume nonlinear material properties and consider the tendon to be frictionless (i.e. Eq. 3.8 $\mu = 0$)

$$\theta_j = \frac{(r_i + \bar{x}_j)h_j}{E_j I_j} F_p. \tag{4.4}$$

Note that the second set of assumptions are the same used in prior modeling (as we saw in Section 2.2), and that under these assumptions, wrist deflection can be treated as a pure elastic beam bending problem; i.e., notch angles can be calculated with Eq. (3.4). To ensure a

Table 4.3: *Model RMSE (degrees) for each notch for wrists A, B, and C.*

Notch	Wrist A	Wrist B	Wrist C
1	1.80	0.43	2.47
2	1.32	0.41	1.49
3	1.01	0.39	1.15
4	0.84	0.57	0.79
5	0.89	0.57	—

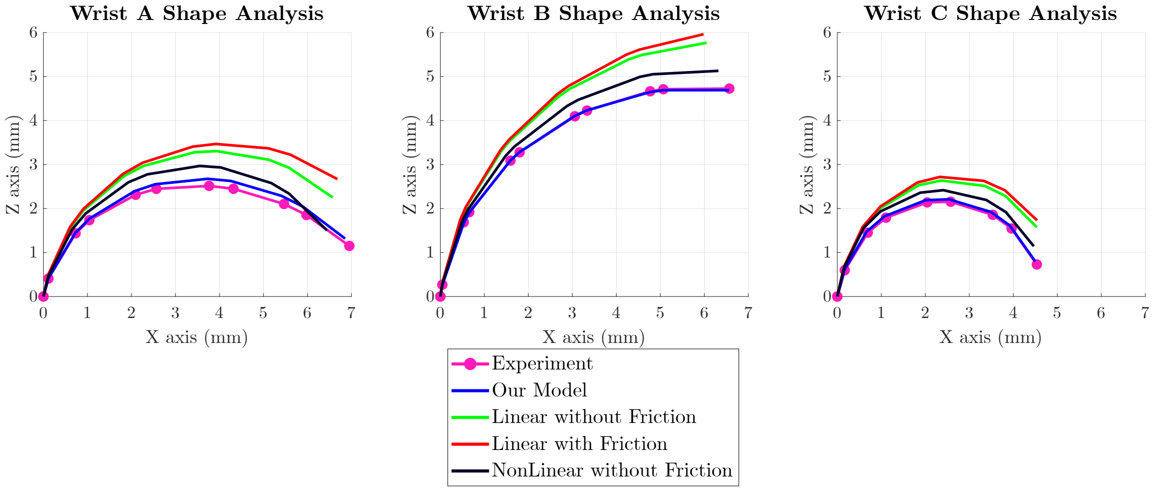

Figure 4.4: *Sample wrist shapes observed during experimentation, along with the wrist shapes predicted by three different models. The model we propose in this thesis (Non-Linear with Friction) predicts the wrist shape almost exactly, while models assuming linear material properties generally provide a higher tracking error.*

fair comparison with our model, we repeated the material identification procedure described in Section 4.3 to identify a value of elastic modulus that yields the best tracking accuracy for these three simpler models.

Results are summarized in Fig. 4.4. It can be observed that the shape of the wrist estimated by Eq. (3.8) (blue line) matches the experimental wrist shape almost exactly. Conversely, assuming linear material properties will generally produce a higher tracking error. Assuming nonlinear material properties but removing friction produces closer estimates, but without friction cannot accurately model the different notch bending rates, causing inaccuracy.

Fig. 4.5 summarizes the tip tracking RMSEs afforded by each of the three models under consideration. These results further demonstrate the higher accuracy of our model (average RMSE: 0.30 mm) compared to simpler models (average RMSEs: 0.91 mm, 0.88 mm, and 0.41 mm, respectively).

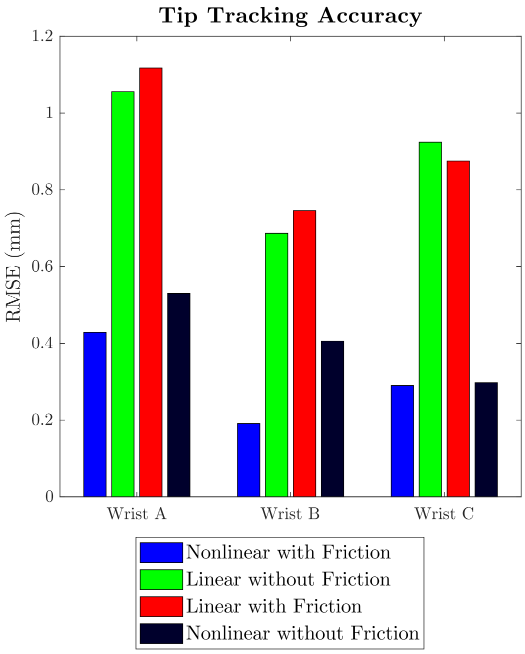

Figure 4.5: *Tip tracking accuracy (Root-Mean-Square Error) of three different models calculated on Wrists A, B, and C.*

CHAPTER 5

DISCUSSION AND FUTURE OUTLOOK

The model presented in this thesis aims to include the effects of tendon friction and material nonlinearity to enhance the tracking accuracy of notched-tube continuum wrists. The model was verified through experiments on three different Nitinol wrists, each designed to achieve a different bending profile. By relaxing the assumptions made in prior work that the tendon is frictionless and that the material of the wrist is linearly elastic, our model can predict the disparate loading conditions at each notch, and therefore accurately capture the actual shape of notched-tube wrists.

By observing the Force/Deflection plots for Wrists A and B in Fig. 4.3, the effects of tendon friction manifest as differences in slope for each notch under loading. We observe that, for more distal notches, parasitic capstan friction effects ultimately reduce the effective moment seen by each notch, thereby reducing deflection for a given tendon force. The fidelity of our model is especially well illustrated in the Force/Deflection plots for Wrist C in Fig. 4.3, where the effects of tendon friction and material nonlinearity on the resulting kinematics are abundantly clear. For an input force of 1 N, notches 1 and 2 remain in the linear elastic regime, whereas notches 3 and 4 have transitioned to superelastic, as indicated by the abrupt increase in slope. Our model matches the experimental data extremely well, and a simpler model relying on linear elastic material assumptions would not be able to capture this phenomenon.

Although we did not conduct experiments with varying diameters, we hypothesize that in certain cases of large tube diameters, the different notch bending rates may not occur for two reasons: firstly, the material may be purely linear (not Nitinol), and secondly, the friction between the tendon and the tube may be negligible compared to the bending stiffness of the tube, EI. The large differences in bending rate we see in nitinol tubes is due to Nitniol's nonlinearities amplifying the small differences created by friction. So a purely elastic material will not see as large of a difference between each notch. Additionally, if the bending stiffness of the material is large enough (increasing with tube size), friction's effect will be lowered even more.

The fabrication process of Nitinol tubes can vary extensively between manufacturers which necessitates the characterization of material properties for a given tube. Our material identification process provided values for the wrist samples we used, which were all cut from the same Nitinol tube, however, future samples may need to undergo the same material identification process.

The algorithm is relatively complex compared to traditional forward kinematics because both θ_j and E_{eff} must be solved numerically. In our implementation, the effective modulus converged in less than 100 iterations, and θ_j converged in 10. This means for each notch we ran 1000 iterations of the gradient descent, with a worst-case complexity scaling linearly with the number of notches $O(n)$. Since there is a one-to-one relationship between the input force and the tube position, a lookup table could easily be generated to store the relationship between the force on the tendon and the bending angles of the tube or even the position of the tube. This would provide fast computation and a relatively granular resolution.

5.1 Future Work

By modeling both friction and material nonlinearities, this work provides a foundation for future research in the simulation and design of notched-tube continuum wrists. Simulations concerned with reachability or path planning can use this model to more accurately determine the position of the tube, the path it will follow, and any collisions that may occur. Furthermore, as we have shown, our model will accurately predict the notch closure sequence for tubes with non-uniform geometry. The process can be inverted to design the notch geometry for a tube based on a desired notch closure sequence. This enables the design of tubes to account for patient-specific anatomy or specific curvature profiles for intravenous and intraluminal navigation.

Additional modeling could be done to account for the wrist "unbending" (i.e., the kinematics when a tendon relaxes and the tube is allowed to return to its original shape). It was noted during experimentation that the behavior of the wrist when the tendon was relaxed was not simply the inverse of applying tension to the tendon. For example, for a uniformly designed wrist, the proximal notches close before the distal notches when tension is applied to the tendon. We hypothesized, based on the inverse of the model, that the proximal notches would open last as the tendon is relaxed. However, we observed that the proximal notches opened first. We believe this is due to, again, a combination of material nonlinearities and friction. The stress-strain curve of Nitinol changes between loading and unloading, so we would need to create an approximation for the unloaded case. Additionally, our use of the capstan model has varying behavior for unloading and loading. As the tube is bending, the loading force on the tendon for the capstan comes from pulling on the tendon and the holding force comes from the tube. When unloading the tendon, the opposite effect will actually occur; the tube will be applying the loading force on the tendon and the holding force will be the force maintaining tension on the tendon.

Another avenue of extension for this work could be by incorporating a rotation between the notches of a tube which would allow the tube to bend out of plane. Currently, our model assumes that the tendon maintains contact with the tube, and the force applied by the tendon is strictly along the z axis of the tube. If we incorporate rotations among the notches, these two assumptions would have to be relaxed, and a more complex model would need to be created.

A potential source of error in the model is the assumption that the entire notch will transition from linear-elasticity to super-elasticity once the strain in the notch reaches a specific threshold. This is best demonstrated by the small error we see in accurately predicting the strain transition value for Wrist C which has a varying backbone thickness. The strain thresholds for the first two notches are underestimated, while those of the most proximal are overestimated. For beam bending, the entire beam does not experience the same amount of strain. Fibers closer to the neutral bending plane will experience strains approaching zero while fibers closer to the outer edge of the beam will experience the maximum amount of strain. When our model transitions from the linear elastic region to the superelastic region, in reality, only the outer fibers of the notch are actually transitioning. Our approximation of Nitinol's material nonlinearity also loses accuracy the more a notch bends which is demonstrated in Wrists A and B. Wrist B, which has the smallest bending angle per notch (18 degrees) has higher accuracy than Wrist A (30 degrees per notch). Our linear approximation of the effective modulus is still an underestimate of the strain energy in the system that becomes more inaccurate the more strain (and hence the larger the bending angle) the notch experiences. Future work would investigate whether the tracking performance of our model can be improved further by accounting for strain variation throughout the notch cross-section and its resulting effect on the notch modulus.

We noticed during experimentation that the tendon thickness played a vital role in the behavior of the wrist. A thicker tendon would produce substantially different results than the 0.1 mm tendon we used for the experiments. Specifically, a thicker tendon would require more force to close the notches. In extreme cases, the tendon could prevent notches from fully closing. Our model assumes the strain energy in the system is entirely determined by the bending angle of the notch, however, a thick enough tendon could store a non-negligible amount of strain energy. Our model implicitly accounted for the effect of tendon thickness when we identified the material properties of the wrist, but changing the tendon thickness would then result in different material properties. To further improve the model, we would investigate the strain energy experienced by the tendon and how it contributes to the notch deflection. Modeling the tendon would build a basis for accounting for the stiffness of tools passed through the wrist. Notched tube wrists are usually designed to have a tool passed through the open lumen, like a laser fiber. This tool would have its own stiffness, similar to the tendon, that would impact the bending of the wrist.

With these considerations, a more complete model describing the internal forces of the wrist would be created, but the position of the tube can still be influenced by external factors. With visual servoing, it may then be possible to estimate the external or contact forces being applied to the tube. The first step would be to perform an analysis similar to what was done in [4], but extend the work to tube positions that do not start initially straight. This would provide a measure of how much additional deflection will occur from external forces applied to an actuated tube. From here, the position of the tube, actuation force, and a relationship between deflection and external forces could be used to determine the external forces being applied to the tube.

If the ultimate goal is a full dynamic model representing the motion of the notched wrist given a pulling force on the tendon, the Cosserat rod model becomes an attractive option. Given the design of the tube, a piecewise function for the second moment of area could be used to account for the notches in the tube similar to [4]. Additionally, a more extensive identification of the material properties of Nitinol would be required.

5.2 Concluding Remarks

As the use of asymmetric notched-tube wrists in robotic minimally invasive surgeries increases, it is important to have accurate models for the simulation and actuation of these devices. Currently available models for asymmetric notched-tube wrists assume that the actuating tendon is frictionless and the material is linear elastic. In this thesis, we presented a mechanics-based model which relaxes these assumptions in order to determine the deflection of the notches individually. We modeled the frictional losses using a capstan friction model and accounted for the non-linear material properties using a secant modulus. The result of our modeling is a system of transcendental equations that can be numerically solved to calculate the deflection of each notch in a wrist based on the actuation force. Experimental data was gathered using three wrists with varying geometries and the proposed model was shown to outperform prior models in accurately predicting the wrist deflection.

BIBLIOGRAPHY

[1] J. Burgner-Kahrs, C. D. Rucker, and H. Choset, "Continuum robots for medical applications: A survey," *IEEE Transactions on Robotics*, vol. 31, no. 6, pp. 1261–1280, 2015.

[2] P. J. Swaney, P. A. York, H. B. Gilbert, J. Burgner-Kahrs, and R. J. Webster, "Design, fabrication, and testing of a needle-sized wrist for surgical instruments," *Journal of medical devices*, vol. 11, no. 1, p. 014501, 2017.

[3] R. J. Webster and B. A. Jones, "Design and kinematic modeling of constant curvature continuum robots: A review," *The International Journal of Robotics Research*, vol. 29, no. 13, pp. 1661–1683, 2010.

[4] K. W. Eastwood, H. Azimian, B. Carrillo, T. Looi, H. E. Naguib, and J. M. Drake, "Kinetostatic design of asymmetric notch joints for surgical robots," in *2016 IEEE/RSJ International Conference on Intelligent Robots and Systems (IROS)*, pp. 2381–2387, IEEE, 2016.

[5] Investor Relations, "Intuitive announces preliminary fourth quarter and full year 2019 results," Jan 2020.

[6] S. Pattanshetti, R. Sandström, A. Kottala, N. M. Amato, and S. C. Ryu, "Feasibility study of robotic needles with a rotational tip-joint and notch patterns," in *2019 International Conference on Robotics and Automation (ICRA)*, pp. 1534–1540, IEEE, 2019.

[7] K. W. Eastwood, P. Francis, H. Azimian, A. Swarup, T. Looi, J. M. Drake, and H. E. Naguib, "Design of a contact-aided compliant notched-tube joint for surgical manipulation in confined workspaces," *Journal of Mechanisms and Robotics*, vol. 10, no. 1, p. 015001, 2018.

[8] F. Alambeigi, Y. Wang, S. Sefati, C. Gao, R. J. Murphy, I. Iordachita, R. H. Taylor, H. Khanuja, and M. Armand, "A curved-drilling approach in core decompression of the femoral head osteonecrosis using a continuum manipulator," *IEEE Robotics and Automation Letters*, vol. 2, no. 3, pp. 1480–1487, 2017.

[9] P. A. York, P. J. Swaney, H. B. Gilbert, and R. J. Webster, "A wrist for needle-sized surgical robots," in *2015 IEEE International Conference on Robotics and Automation (ICRA)*, pp. 1776–1781, May 2015.

[10] J. Liu, B. Hall, M. Frecker, and E. W. Reutzel, “Compliant articulation structure using superelastic nitinol,” *Smart materials and structures*, vol. 22, no. 9, p. 094018, 2013.

[11] J. A. Bell, C. E. Saikus, K. Ratnayaka, V. Wu, M. Sonmez, A. Z. Faranesh, J. H. Colyer, R. J. Lederman, and O. Kocaturk, “A deflectable guiding catheter for real-time mri-guided interventions,” *Journal of Magnetic Resonance Imaging*, vol. 35, no. 4, pp. 908–915, 2012.

[12] D. Wei, Y. Wenlong, H. Dawei, and D. Zhijiang, “Modeling of flexible arm with triangular notches for applications in single port access abdominal surgery,” in *2012 IEEE International Conference on Robotics and Biomimetics (ROBIO)*, pp. 588–593, IEEE, 2012.

[13] Y. Haga, Y. Muyari, S. Goto, T. Matsunaga, and M. Esashi, “Development of minimally invasive medical tools using laser processing on cylindrical substrates,” *Electrical Engineering in Japan*, vol. 176, no. 1, pp. 65–74, 2011.

[14] M. D. Kutzer, S. M. Segreti, C. Y. Brown, M. Armand, R. H. Taylor, and S. C. Mears, “Design of a new cable-driven manipulator with a large open lumen: Preliminary applications in the minimally-invasive removal of osteolysis,” in *2011 IEEE International Conference on Robotics and Automation*, pp. 2913–2920, IEEE, 2011.

[15] S. C. Ryu, P. Renaud, R. J. Black, B. L. Daniel, and M. R. Cutkosky, “Feasibility study of an optically actuated mr-compatible active needle,” in *2011 IEEE/RSJ international conference on intelligent robots and systems*, pp. 2564–2569, Ieee, 2011.

[16] L. Fichera, N. P. Dillon, D. Zhang, I. S. Godage, M. A. Siebold, B. I. Hartley, J. H. Noble, P. T. Russell, R. F. Labadie, and R. J. Webster, “Through the eustachian tube and beyond: A new miniature robotic endoscope to see into the middle ear.,” *IEEE robotics and automation letters*, vol. 2, no. 3, pp. 1488–1494, 2017.

[17] A. J. Chiluisa, F. J. Van Rossum, J. B. Gafford, R. F. Labadie, R. J. Webster, and L. Fichera, “Computational optimization of notch spacing for a transnasal ear endoscopy continuum robot,” in *2020 International Symposium on Medical Robotics (ISMR)*, pp. 188–194, IEEE, 2020.

[18] J. Gafford, M. Freeman, L. Fichera, J. Noble, R. Labadie, and R. J. Webster, “Eyes in ears: a miniature steerable digital endoscope for trans-nasal diagnosis of middle ear disease,” *Annals of Biomedical Engineering*, vol. 49, no. 1, pp. 219–232, 2021.

[19] A. Swarup, K. W. Eastwood, P. Francis, N. Chayaopas, L. A. Kahrs, C. G. Leonard, J. Drake, and A. James, “Design, prototype development and pre-clinical validation of a novel instrument with a compliant steerable tip to facilitate endoscopic ear surgery,” *Journal of Medical Engineering & Technology*, vol. 45, no. 1, pp. 22–34, 2021. PMID: 33191826.

[20] K. W. Eastwood, A. Swarup, P. Francis, A. N. Alvara, H. Chen, T. Looi, H. E. Naguib, and J. M. Drake, “A steerable neuroendoscopic instrument using compliant contact-aided joints and monolithic articulation,” *Journal of Medical Devices*, vol. 14, no. 2, 2020.

[21] P. Francis, K. Eastwood, V. Bodani, T. Looi, and J. Drake, “Design, modelling and teleoperation of a 2 mm diameter compliant instrument for the da vinci platform,” *Annals of biomedical engineering*, vol. 46, no. 10, pp. 1437–1449, 2018.

[22] P. Francis, K. W. Eastwood, V. Bodani, K. Price, K. Upadhyaya, D. Podolsky, H. Azimian, T. Looi, and J. Drake, “Miniaturized instruments for the da vinci research kit: Design and implementation of custom continuum tools,” *IEEE Robotics & Automation Magazine*, vol. 24, no. 2, pp. 24–33, 2017.

[23] G. Gerboni, J. D. Greer, P. F. Laeseke, G. L. Hwang, and A. M. Okamura, “Highly articulated robotic needle achieves distributed ablation of liver tissue,” *IEEE robotics and automation letters*, vol. 2, no. 3, pp. 1367–1374, 2017.

[24] M. Chauhan, N. Deshpande, D. G. Caldwell, and L. S. Mattos, “Design and modeling of a three-degree-of-freedom articulating robotic microsurgical forceps for trans-oral laser microsurgery,” *Journal of Medical Devices*, vol. 13, no. 2, p. 021006, 2019.

[25] D. C. Rucker, *The Mechanics of Continuum Robots: Model-Based Sensing and Control*. PhD thesis, Vanderbilt University, 2201 West End Ave, Nashville, TN 37235, 10 2011. An optional note.

[26] R. Hibbeler, *Mechanics of Materials*. Pearson, 2016.

APPENDIX A

CALCULATING THE NEUTRAL BENDING PLANE

The neutral bending plane for a single notch in an asymmetric notched-tube wrist, $\bar{x}$, is located at the centroid of the notch's horizontal cross-section. The cross-section's centroid and shape is determined by the cutting pattern used: either an off-axis cut or an on-axis cut. An off-axis cut is one where the cut direction is perpendicular to x-axis of the tube see in Fig. A.1. An on-axis cut is one where the cut direction is along the radial axis of the tube seen in Fig. A.2. With both cut types, $\bar{x}$ can be found using the following geometric relationship:

$$\bar{x} = \frac{\bar{x}_o A_o - \bar{x}_i A_i}{A_o - A_i}. \tag{A.1}$$

where the Areas, A_o and A_i, and their respective centroids, $\bar{x}_o$ and $\bar{x}_i$, are defined by the geometry of the cut in the following sections.

A.1 Off-Axis Cutting

An off-axis cutting pattern, shown in Fig. A.1 was used in the wrists developed by York and Swaney et. al. [2]. For an off-axis cutting pattern, A_o and A_i are circular segments. To determine their area and centroids, we first define the angle of the segments, ϕ_o and ϕ_i.

$$\phi_o = 2\arccos(\frac{g - r_o}{r_o}) \quad \phi_i = 2\arccos(\frac{g - r_o}{r_i}) \tag{A.2}$$

$$A_o = \frac{r_o^2(\phi_o - \sin(\phi_o))}{2} \quad A_i = \frac{r_i^2(\phi_i - \sin(\phi_i))}{2} \tag{A.3}$$

$$\bar{x}_o = \frac{4r_o \sin^3(\frac{1}{2}\phi_o)}{3(\phi_o - \sin(\phi_o))} \quad \bar{x}_i = \frac{4r_i \sin^3(\frac{1}{2}\phi_i)}{3(\phi_i - \sin(\phi_i))} \tag{A.4}$$

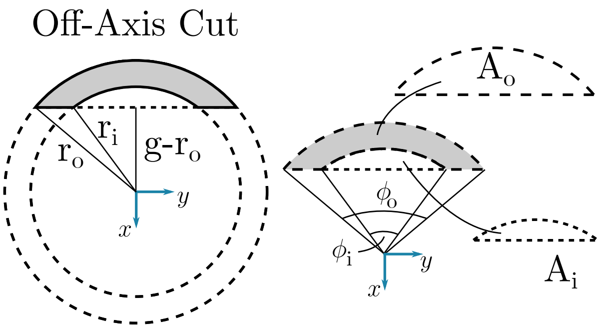

Figure A.1: *A visual representation of off-axis cutting and the resulting circular segments A_o and A_i.*

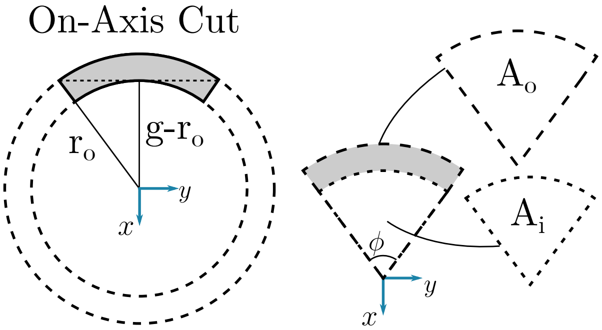

Figure A.2: *A visual representation of on-axis cutting and the resulting circular sectors A_o and A_i.*

A.2 On-Axis Cutting

An on-axis cutting pattern, shown in Fig. A.2 was used for the wrists used in the experimental verification. For an on-axis cutting pattern, A_o and A_i are circular sectors. To determine their area and centroids, we first define the angle of the sectors, ϕ.

$$\phi = 2\arccos(\frac{g_j - r_o}{r_o}) \tag{A.5}$$

$$A_o = \frac{\phi}{2}r_o^2 \qquad A_i = \frac{\phi}{2}r_i^2 \tag{A.6}$$

$$\bar{x}_o = \frac{2r_o \sin\frac{\phi}{2}}{3\frac{\phi}{2}} \qquad \bar{x}_i = \frac{2r_i \sin\frac{\phi}{2}}{3\frac{\phi}{2}} \tag{A.7}$$

APPENDIX B

NOTCH DEFLECTION ALGORITHM

Algorithm 1 Runs the gradient descent algorithm to determine the notch angles.

```
procedure GETNOTCHANGLE($F_p$)
    $\Theta_{last} = [0]$    ; Initialize deflection vector
    while $\epsilon < 10^{-6}$ and $m < maxiter$ do
        for $j \leftarrow 1, n$ do
            $E_{eff} = E_{lin}$    ; initialize effective modulus
            Solve $F_j(F_p, \Theta_{last})$ ; estimate friction force from last deflection vector
            Solve $M_j(F_j)$    ; estimate moment
            while $\epsilon_E > 10^{-6}$ and $k < maxiter$ do
                Solve $\theta_j(M_j, E_{eff})$
                Solve $\varepsilon(\theta_j)$, $\sigma(\varepsilon)$    ; estimate stress from nonlinear curve
                $E_{new} = E_{eff} - \eta(E_{eff} - \sigma/\varepsilon)$    ; gradient descent step
                $\epsilon_E = (E_{new} - E_{eff})/E_{eff}$    ; compute percent change
                $E_{eff} = E_{new}$
                $k++$
        $\Theta = [\theta_1, \theta_2, ..., \theta_n]^T$    ; save notch angle vector
        $\epsilon = |\Theta| - |\Theta_{last}|$    ; compute norm error
        $\Theta_{last} = \Theta_{update}$
        $m++$
```